


Article

The Effect of Cation Incorporation on the Elastic and Vibrational Properties of Mixed Lead Chloride Perovskite Single Crystals

Syed Bilal Junaid, Furqanul Hassan Naqvi and Jae-Hyeon Ko * 

School of Nano Convergence Technology, Nano Convergence Technology Center, Hallym University, Chuncheon 24252, Republic of Korea; 43497@hallym.ac.kr (S.B.J.); furqan hassan@hallym.ac.kr (F.H.N.)

* Correspondence: hwangko@hallym.ac.kr

Abstract: In recent years, there have been intense studies on hybrid organic–inorganic compounds (HOIPs) due to their tunable and adaptable features. This present study reports the vibrational, structural, and elastic properties of mixed halide single crystals of $MA_xFA_{1-x}PbCl_3$ at room temperature by introducing the FA cation at the A-site of the perovskite crystal structure. Powder X-ray diffraction analysis confirmed that its cubic crystal symmetry is similar to that of $MAPbCl_3$ and $FAPbCl_3$ with no secondary phases, indicating a successful synthesis of the $MA_xFA_{1-x}PbCl_3$ mixed halide single crystals. Structural analysis confirmed that the FA substitution increases the lattice constant with increasing FA concentration. Raman spectroscopy provided insight into the vibrational modes, revealing the successful incorporation of the FA cation into the system. Brillouin spectroscopy was used to investigate the changes in the elastic properties induced via the FA substitution. A monotonic decrease in the sound velocity and the elastic constant suggests that the incorporation of large FA cations causes distortion within the inorganic framework, altering bond lengths and angles and ultimately resulting in decreased elastic constants. An analysis of the absorption coefficient revealed lower attenuation coefficients as the FA content increased, indicating reduced damping effects and internal friction. The current findings can facilitate the fundamental understanding of mixed lead chloride perovskite materials and pave the way for future investigations to exploit the unique properties of mixed halide perovskites for advanced optoelectronic applications.

Keywords: lead halide perovskites; $MA_{1-x}FA_xPbCl_3$; Raman spectroscopy; Brillouin spectroscopy



Citation: Junaid, S.B.; Naqvi, F.H.; Ko, J.-H. The Effect of Cation Incorporation on the Elastic and Vibrational Properties of Mixed Lead Chloride Perovskite Single Crystals. *Inorganics* **2023**, *11*, 416. <https://doi.org/10.3390/inorganics111100416>

Academic Editors: Sake Wang, Minglei Sun and Nguyen Tuan Hung

Received: 28 September 2023

Revised: 13 October 2023

Accepted: 17 October 2023

Published: 22 October 2023



Copyright: © 2023 by the authors. Licensee MDPI, Basel, Switzerland. This article is an open access article distributed under the terms and conditions of the Creative Commons Attribution (CC BY) license (<https://creativecommons.org/licenses/by/4.0/>).

1. Introduction

Hybrid organic–inorganic perovskites (HOIPs), particularly 3D perovskites denoted as the formula ABX_3 , have recently attracted considerable attention due to their versatile properties [1–6]. Here, X denotes halide anions (I^- , Br^- , Cl^-) located inside corner-sharing BX_6 octahedra, where B denotes divalent metal cations (Pb^{2+} , Sn^{2+}), and A represents monovalent cations (FA^+ , MA^+ , Cs^+). In particular, perovskites, such as $MAPbX_3$ ($MA = CH_3NH_3^+$, methylammonium) and $FAPbX_3$ ($FA = CH(NH_2)_2^+$, formamidinium), have attracted significant attention due to their remarkable photovoltaic performance and exceptional optical and photoluminescent properties. Additionally, their low-cost solution processability enhances their potential, making them promising candidates for implementation in solar cells, light-emitting diodes, and photodetectors [1–12].

$APbX_3$ compounds have been extensively investigated as highly effective materials for photovoltaics [7,8,12]. Their power conversion efficiencies have exceeded 25% throughout the last ten years, largely due to their high absorption coefficients, modifiable band gaps, and other contributing factors [13–17]. Nonetheless, the features of HOIPs can be significantly altered via the cation and anion compositions and structural phase transitions, leading to promising opportunities for further optimization [18–20]. In particular, $FAPbX_3$ compounds ($X = I, Br, Cl$) within the HOIPs have attracted considerable attention due

to their narrower and more preferable band gap, improved thermal stability at higher temperatures, and a more symmetrical crystal structure in contrast to their counterparts with MA [21–24]. Within the MAPbX_3 family, MAPbCl_3 has wide-ranging applications in ultraviolet (UV) photodetection due to its wide band gap of 2.88 eV [25]. This compound undergoes two distinct phase transitions with decreasing temperature from cubic to tetragonal at 163 K and then to orthorhombic phases at 159 K [26,27]. In contrast, FAPbCl_3 is a distinctive compound among the FAPbX_3 compounds due to its high stability, which has proven to be critical in the development of highly sensitive ammonia gas sensors [28] and polymer solar cells with anode interfacial layers (AIL) that have achieved power conversion efficiency (PCE) of 8.75% [29]. Moreover, the ambipolar transport properties of FAPbCl_3 also play a significant role in the fields of UV detection and optoelectronics [29,30]. Differential scanning calorimetry (DSC) and quasi-elastic neutron scattering (QENS) experiments indicate that it undergoes phase transitions from cubic to tetragonal at 271 K and then from tetragonal to orthorhombic phase at 258 K [31,32]. Furthermore, only a few density functional theory (DFT) studies thus far [33–35] have focused on their electronic, optical, and elastic properties. However, no research studies have yet integrated mixed A site cation composition for lead chloride. Therefore, our aim is to fill this research gap by analyzing the mixed $\text{MA}_x\text{FA}_{1-x}\text{PbCl}_3$ system.

The integration of mixed A-site cation compositions, such as hybrid FA/MA single crystals, has been used to improve device performances [36–41]. These compositional variations provide clear benefits, including the ability to precisely adjust band gaps and exhibit remarkable stability under different stress conditions, resulting in the successful demonstration of the most successful solar cells using these mixed A-site cation perovskites to date [36–41]. In regard to band gap tuning, studies have revealed a significant redshift in the fundamental band gap when FA replaces MA in MAPbI_3 [42]. Researchers have employed various techniques, such as photoluminescence (PL) measurements [43], absorption [44], diffuse reflectance [45], and ellipsometry spectra [46], to investigate this phenomenon. Furthermore, hybrid $\text{FA}_x\text{MA}_{1-x}\text{PbI}_3$ perovskites were investigated in Raman and PL studies. The resulting temperature–composition phase diagram confirms a slight redshift in the fundamental band gap when replacing MA cations with FA cations [47].

In regard to improved photovoltaic applications, recent studies show that MAPbI_3 achieves impressive power conversion efficiencies (PCEs) exceeding 17% [6,9]. Nevertheless, they face challenges like thermal and moisture instability issues [7,10–12]. Similarly, FAPbI_3 perovskite also shows potential as a photovoltaic material due to its narrower bandgap (E_g) of 1.48 eV, aligning more closely with the Shockley–Queisser ideal bandgap of approximately 1.40 eV for single-junction solar cells. This alignment indicates the possibility of achieving even higher PCEs [48,49]. However, there are challenges, particularly the undesirable creation of a yellow non-perovskite δ -phase during the annealing process, which hinders the efficiency of resulting photovoltaic solar cells (PVSCs) due to their insulating properties. To overcome these obstructions inherent within initial perovskite materials, researchers have explored the concept of mixing A-site cations as a strategy to achieve improved PCEs. Grätzel et al. successfully demonstrated an approach to achieving higher PCEs in perovskite solar cells [23]. In particular, they synthesized the perovskite $\text{MA}_{0.6}\text{FA}_{0.4}\text{PbI}_3$ via the partial substitution of MA^+ ions with FA^+ ions in MAPbI_3 , resulting in an enhanced efficiency compared to parent perovskites [23].

The use of cation–halide mixtures is a widely used method to stabilize the cubic perovskite structure at operational temperatures [37,50–53]. In particular, FA-dependent perovskites, such as FAPbI_3 , typically undergo a phase transition from the cubic α -phase to the undesired hexagonal δ -phase at room temperature, affecting its photovoltaic behavior. However, the introduction of cation–halide mixtures helps to stabilize the cubic phase [37,50–53]. Furthermore, studies on mixed $\text{MA}_{1-x}\text{FA}_x\text{PbBr}_3$ hybrids have used methods such as specific heat and differential scanning calorimetry to investigate the phase transition behavior. These studies have revealed a significant reduction in phase transition temperatures and increased the stability of the cubic phase caused by the A-site

mixing [54]. These findings emphasize the considerable influence of mixed A-site cations on the characteristics of lead halide perovskites.

Our research aims to investigate mixed $\text{MA}_x\text{FA}_{1-x}\text{PbCl}_3$ single crystals, which, to the best of our knowledge, have not been studied before. We successfully analyzed the changes in the optical and acoustic phonon modes induced via the FA substitution at room temperature. We introduced 30% and 40% FA at the A-site cation of MAPbCl_3 and studied their properties using Raman and Brillouin spectroscopic techniques. The cation stoichiometries (i.e., x values) were precisely determined using nuclear magnetic resonance (NMR) spectroscopy. Raman spectroscopy was used to investigate optical phonon modes in the low-frequency range, corresponding to lattice vibrations. The observed decrease in wavenumber with increasing FA content indicates changes in the Pb-Cl bond strength within the lattice. Furthermore, Brillouin spectroscopy was used to obtain acoustic phonon velocities and associated elastic constants. Our results indicate that these parameters decrease with increasing FA content, suggesting that the lattice rigidity is reduced due to the larger cation radius of the FA cation compared to the MA cation, resulting in the lattice distortion and the softer lattice structure.

2. Results and Discussion

The synthesized samples were initially analyzed using solid-state ^1H NMR spectroscopy to determine the exact FA/MA ratios. Figure 1 illustrates the ^1H magic-angle spinning (MAS) spectra for $\text{MA}_x\text{FA}_{1-x}\text{PbCl}_3$ ($x = 1, 0.7, 0.6$) single crystals. The spectrum of the MAPbCl_3 composition indicates two distinguishable peaks at 6.52 and 3.29 ppm, with a ratio of 1:1. Interestingly, the signals of the $-\text{NH}_3^+$ and $-\text{CH}_3$ protons, which have previously been linked to the MAPbX_3 series ($X = \text{I}, \text{Br}, \text{Cl}$) [55], were correlated with these peaks. The NMR data analysis indicated a discrepancy between the real compositions of the samples and the nominal compositions employed during synthesis. The $\text{MA}_x\text{FA}_{1-x}\text{PbCl}_3$ had values of x at 1, 0.87, and 0.77 with percentage errors of 28% and 24% for the mixed systems, respectively. It is worth noting that the MA content decreased significantly in the mixed crystal compared to the starting ratio. This emphasizes the importance of monitoring the actual MA/FA ratio for this and similar systems after the materials are synthesized. The discrepancy between the nominal and measured stoichiometries may be due to the different solubilities and reactivities of the MA and FA precursors in the solution.

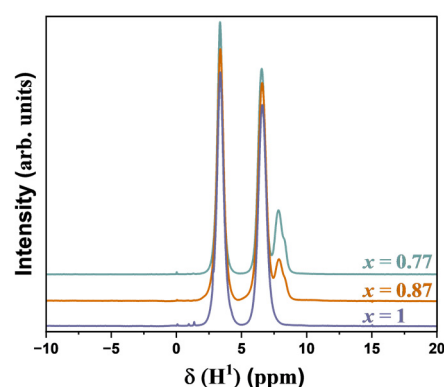


Figure 1. Solid-state (^1H) NMR spectra of the $\text{MA}_x\text{FA}_{1-x}\text{PbCl}_3$ ($x = 1, 0.87, 0.77$) single crystals.

The powder X-ray diffraction (PXRD) pattern of $\text{MA}_x\text{FA}_{1-x}\text{PbCl}_3$ with varying compositions is shown in Figure 2. The diffraction pattern consistent with the cubic XRD patterns of MAPbCl_3 [56] and FAPbCl_3 [57] emphasizes the crystallographic cubic structure of the synthesized compounds. Notably, the absence of additional peaks and peak splitting in the PXRD pattern of the mixed crystals at room temperature confirms the high-quality cubic crystal symmetry ($Pm\bar{3}m$) shared with MAPbCl_3 and FAPbCl_3 [56,57].

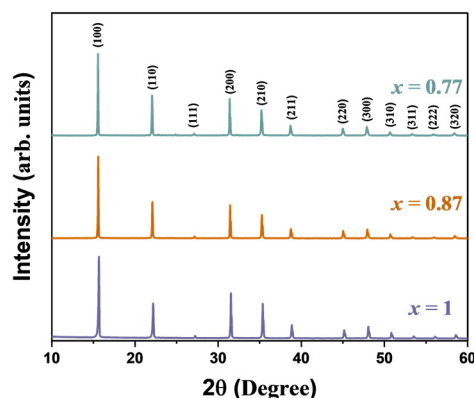


Figure 2. PXRD patterns of synthesized $\text{MA}_x\text{FA}_{1-x}\text{PbCl}_3$ ($x = 1, 0.87, 0.77$) single crystals.

Figure 3 shows the changes in the lattice constant, the unit cell volume, and the density as a function of FA content within the $\text{MA}_x\text{FA}_{1-x}\text{PbCl}_3$ system. Figure 3a,b show that the lattice constant and the unit cell volume exhibit a linearly increasing trend with increasing FA content. This observation supports a strong link between structural changes induced via the FA substitution and their influence on material properties. There is an increase in the lattice constant from 5.67 to 5.69 Å with increasing FA content. This increase in the lattice constant and the unit cell volume can be attributed to the weakening of electrostatic forces resulting from the change in the atomic packing. In particular, the substitution of smaller MA cations by larger FA cations within the perovskite structure causes structural distortion and a decrease in the atomic packing density, as shown in Figure 3c. The absolute values of all these parameters are reported in Table 1.

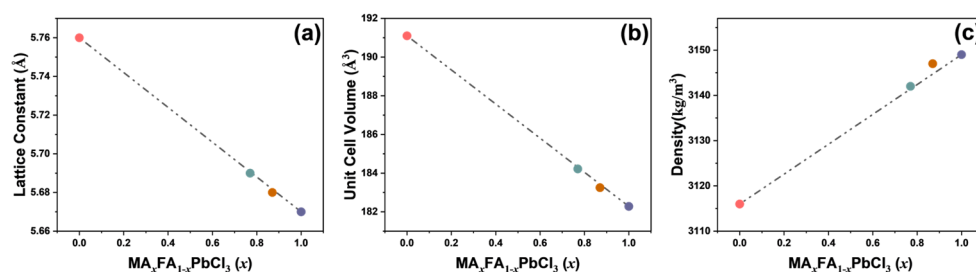


Figure 3. (a) Lattice constant, (b) unit-cell volume, and (c) density of $\text{MA}_x\text{FA}_{1-x}\text{PbCl}_3$ ($x = 1, 0.87, 0.77$) single crystals. The lattice constant of FAPbCl_3 was taken from ref. [57].

Table 1. Summary of crystallographic and physical properties for $\text{MA}_x\text{FA}_{1-x}\text{PbCl}_3$ ($x = 1, 0.87, 0.77$) single crystals. Refractive indices for MAPbCl_3 [58] and FAPbCl_3 [33] were interpolated to get values for all mixed compositions. The lattice constant of FAPbCl_3 was taken from ref. [57].

Composition	Lattice Parameter (Å)	Unit-Cell Volume (Å ³)	Refractive Index (<i>n</i>)	Density (kg/m ³)
MAPbCl_3	5.67	182.28	1.90 [58]	3149
$\text{MA}_{0.87}\text{FA}_{0.13}\text{PbCl}_3$	5.68	183.25	1.93	3147
$\text{MA}_{0.77}\text{FA}_{0.23}\text{PbCl}_3$	5.69	184.22	1.95	3142
FAPbCl_3	5.76 [57]	191.10	2.10 [33]	3116

Raman spectroscopy has been employed for exploring the vibrational dynamics of the mixed lead halide perovskite material, as it gives us insights into the lattice dynamics, phonon modes, and other material properties. Figure 4a–c displays the Raman spectra of $\text{MA}_x\text{FA}_{1-x}\text{PbCl}_3$ single crystals at room temperature, covering a broad range of wavenumbers from 10 to 3500 cm^{-1} . For the sake of clarity, this study categorizes the data into low,

medium, and high wavenumber regions. The Raman spectra exhibit significant peaks that correspond to lattice vibrational modes and internal modes of the constituent cations. In particular, these cations are the MA cation (for $x = 1$) and the MA/FA cations (for $x = 0.87, 0.77$). It is worth noting that $\text{MA}_x\text{FA}_{1-x}\text{PbCl}_3$ ($x = 0.87, 0.77$) produces additional peaks in the frequency domain at 522 cm^{-1} , 1117 cm^{-1} , 1396 cm^{-1} , 1713 cm^{-1} , 3228 cm^{-1} , and 3336 cm^{-1} . These peaks correspond to the bending mode of the FA^+ cation [11,59], the symmetric stretching of CN [11,59], the rocking mode of NH_2 [11,59,60], the asymmetric stretching of NH_2 [60,61], and the stretching of NH_2 (3228 cm^{-1} , 3336 cm^{-1}) [60–62], respectively. This provides strong evidence for the successful substitution of the FA cation within the crystal lattice.

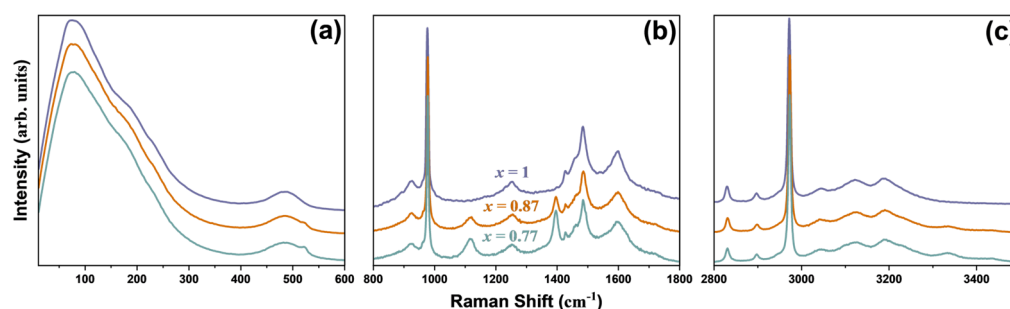


Figure 4. Room temperature Raman spectra of $\text{MA}_x\text{FA}_{1-x}\text{PbCl}_3$ ($x = 1, 0.87, 0.77$) single crystals in (a) $10\text{--}600\text{ cm}^{-1}$, (b) $800\text{--}1800\text{ cm}^{-1}$, and (c) $2800\text{--}3500\text{ cm}^{-1}$ wavenumber ranges.

The peak positions for all the observed vibrational modes were determined in terms of the curve fitting analysis using the Lorentzian function. A graphical representation of this fitting process is provided in the Supplementary Materials, with the resulting individual fitting lines for the Raman spectra recorded at room temperature (Figures S1–S3). The vibrational mode wavenumbers obtained from the fitting analyses are listed, as shown in Table 2, with their respective mode assignments.

Table 2. Mode assignments of Raman peaks of $\text{MA}_x\text{FA}_{1-x}\text{PbCl}_3$ ($x = 1, 0.87, 0.77$) single crystals at room temperature.

MAPbCl_3 (cm^{-1})	$\text{MA}_{0.87}\text{FA}_{0.13}\text{PbCl}_3$ (cm^{-1})	$\text{MA}_{0.77}\text{FA}_{0.23}\text{PbCl}_3$ (cm^{-1})	Mode Assignment
36	36	36	PbCl_6 motion [62,63]
63	62	62	PbCl_6 motion [63]
90	89	88	δ_s (Cl–Pb–Cl) [59]
122	123	123	δ_{as} (Cl–Pb–Cl) [59]
182	177	174	ν_{as} (Pb–Cl) [59,61]
239	232	228	R of MA^+ cation [63]
484	486	485	τ (MA) [64]
	522	522	δ (FA) [11,61]
922	924	923	ρ (MA) [61]
962	962	961	
976	978	978	ν (C–N) [59]
	1117	1116	ν_s (CN) [11,61]
1246	1247	1247	ρ (MA) [59,62]
	1396	1395	ρ (NH_2^+) [11,60,61]
1427	1428	1428	δ_s (CH_3) [59]

Table 2. Cont.

MAPbCl ₃ (cm ⁻¹)	MA _{0.87} FA _{0.13} PbCl ₃ (cm ⁻¹)	MA _{0.77} FA _{0.23} PbCl ₃ (cm ⁻¹)	Mode Assignment
1455	1458	1458	δ_{as} (CH ₃) [59]
1485	1486	1486	δ_s (NH ₃) [59]
1597	1600	1600	δ_{as} (NH ₃) [59]
	1715	1716	ν_{as} (CN) [60,61]
2830	2831	2831	Combination modes [65]
2897	2898	2898	ν_s (C–H) [62]
2947	2949	2948	sym. CH ₃ stretch [65]
2972	2973	2973	ν_{as} (C–H) [59,62,65]
3042	3042	3041	ν_s (CH ₃) [59,62,65]
3120	3120	3118	ν_s (NH ₃) [62]
3189	3190	3190	ν_s (NH ₃) [62]
3221	3229	3228	ν (NH ₂) [60–62]
	3336	3336	ν (NH ₂) [60,61]
	3438	3436	sym. NH ₃ ⁺ stretch [65]

δ : bending; ρ : rocking; ν : stretching; s/as : symmetric/asymmetric; τ : torsion; R: rotation.

Figure 4a shows the low-frequency lattice modes below 600 cm⁻¹, including the characteristic torsional (τ) mode of the MA cation and the characteristic bending (δ) mode of the FA cation. In particular, the bending (δ) mode of the FA cation is more pronounced, indicating a significant effect of the FA inclusion. It is also worth noting that there is a slight reduction in the mode frequencies of the low-frequency lattice modes with increasing FA content. The small reduction in mode frequencies is probably due to the complex interplay between the FA and MA cations, which has a significant effect on the bonding characteristics of the PbCl₆ octahedra. When larger FA cations occupy the MA site, they generate local stress distortions, leading to changes in the lattice behavior and intermolecular angles.

The results for the mid-frequency modes from 800 to 1800 cm⁻¹ are shown in Figure 4b. These vibrational data show that FA has been integrated into the mixed crystal structure, as evidenced in the clear observation of the symmetric stretching mode of CN [11,59] (~1117 cm⁻¹) and the rocking mode of NH₂ [11,59,60] (~1396 cm⁻¹) of FA. The mode intensity tends to increase with increasing FA content as seen in the bending mode of the FA cation. These vibrations demonstrate how cations interact within the crystal lattice and provide valuable insights into the complex nature of localized structural changes resulting from the coexistence of different cationic entities.

The internal modes observed between 2800 and 3500 cm⁻¹ are shown in Figure 4c. Although there are only minor shifts in mode frequencies, new internal modes associated with the stretching of the NH₂ mode [60,61] (~3228 cm⁻¹, 3336 cm⁻¹) appear, revealing the successful integration of the FA cation in the crystal structure. The distinct properties of the FA and MA cations induce a rearrangement of atomic interactions, resulting in local perturbations as evidenced by the spectra.

Overall, the Raman spectroscopy results suggest that small changes in certain Raman modes indicate the presence of local structural distortions within the crystal. These deviations can be attributed to various factors, such as the different ionic radii of the FA and MA cations and their different interactions with the PbCl₆ octahedra. The random substitution of the larger FA cation into the MA site generates local heterogeneous stresses throughout the lattice, which, in turn, affects the lattice dynamics and interactions with neighboring PbCl₆ octahedra and can alter the Pb–Cl bond length and the Pb–Cl–Pb bond angle.

Figure 5 shows the Brillouin spectra at room temperature for the mixed single crystals of $\text{MA}_x\text{FA}_{1-x}\text{PbCl}_3$. Two distinct doublets can be seen in these spectra, corresponding to the longitudinal acoustic (LA) and transverse acoustic (TA) modes. The mode frequencies of both the LA and TA modes shift to lower values as the FA content increases. This phenomenon indicates changes in the elastic properties of the perovskite lattice due to the introduction of FA cations. The larger FA^+ cation leads to extended Pb-Cl bond lengths and weaker bond strengths within the inorganic framework of halide perovskites. Consequently, a softer lattice structure and lower elastic moduli are expected. The Brillouin spectra were fitted using the Voigt function, a convolution of the Gaussian instrumental function, and the Lorentzian phonon response function. The sound velocity (V) can be calculated from the acoustic mode frequency (ν_B) using the following equation:

$$V = \frac{\nu_B \lambda}{2n} \quad (1)$$

where λ is the wavelength of the excitation source (532 nm), and n is the refractive index of the crystal. However, the experimental refractive indices for $\text{MA}_x\text{FA}_{1-x}\text{PbCl}_3$ ($x = 0.87, 0.77$) are not reported. Therefore, approximate refractive indices were obtained via linear interpolation between the experimental value of MAPbCl_3 ($n = 1.90$) [58] and the theoretical value of FAPbCl_3 ($n = 2.10$) [33] obtained from DFT calculations, as shown in Figure S4 in the Supplementary Information. From these data, the longitudinal and transverse sound velocities were obtained and plotted in Figure 6a,b. Over the investigated composition range, the longitudinal and transverse sound velocities show a monotonic decrease with increasing FA content. In particular, for the composition change from $x = 1$ to $x = 0.77$, the longitudinal sound velocity decreases from 3574 m/s to 3471 m/s, and the transverse sound velocity decreases from 1087 m/s to 961 m/s. The increase in the lattice constant, caused via the incorporation of the larger FA cation, seems to be the primary factor contributing to the gradual decrease in the sound velocity. In addition, the reduced dipole moment of the FA cation could lead to lower acoustic phonon velocities. Similar behavior was observed by Ma et al. [66] in the mixed system of $\text{FA}_x\text{MA}_{1-x}\text{PbBr}_3$.

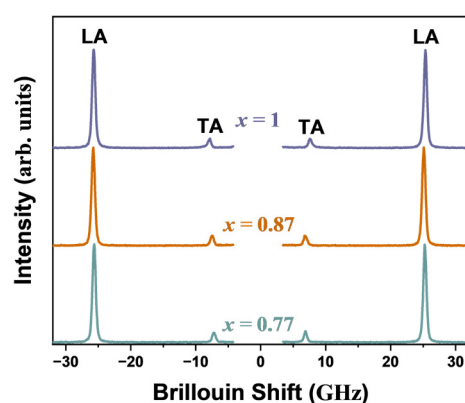


Figure 5. Room temperature Brillouin spectra of $\text{MA}_x\text{FA}_{1-x}\text{PbCl}_3$ ($x = 1, 0.87, 0.77$) single crystals. The LA and the TA denote the longitudinal and the transverse acoustic modes, respectively.

The LA and TA modes observed in this scattering geometry correspond to the elastic constants C_{11} and C_{44} , respectively. These elastic constants can be determined from the sound velocity (V) and the crystal density (ρ) using the following relation:

$$C_{ij} = \rho V^2 \quad (2)$$

The calculated densities for the $\text{MA}_x\text{FA}_{1-x}\text{PbCl}_3$ ($x = 1, 0.87, 0.77$) single crystals are 3149 kg/m³, 3147 kg/m³, and 3142 kg/m³, respectively. These values were determined using the lattice parameter obtained from PXRD and the chemical formula. The elastic

constants C_{11} and C_{44} are shown in Figure 7a,b, respectively. Both C_{11} and C_{44} show a gradual decrease from 40.22 GPa to 37.85 GPa and from 3.72 GPa to 2.90 GPa, respectively, with an increase in FA cations. The results are presented in Table 3, together with the reported values for FAPbCl₃ obtained from DFT calculations.

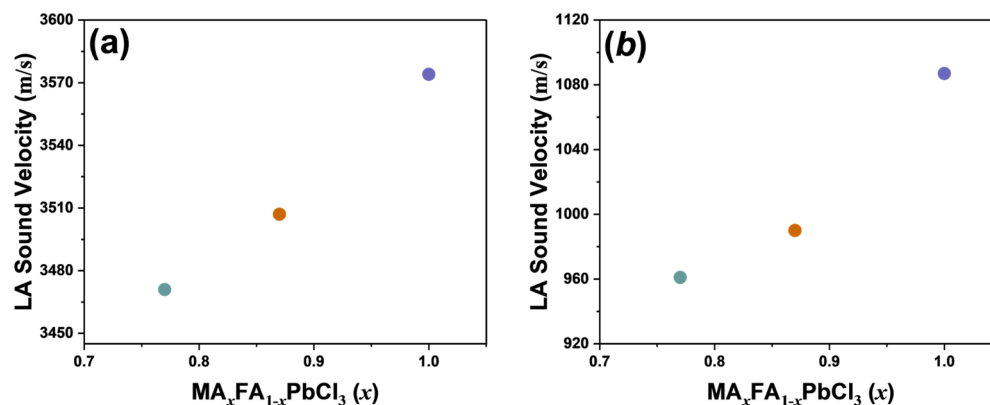


Figure 6. (a) Longitudinal acoustic (LA) and (b) transverse acoustic (TA) sound velocities as a function of composition x in $\text{MA}_x\text{FA}_{1-x}\text{PbCl}_3$ ($x = 1, 0.87, 0.77$) single crystals.

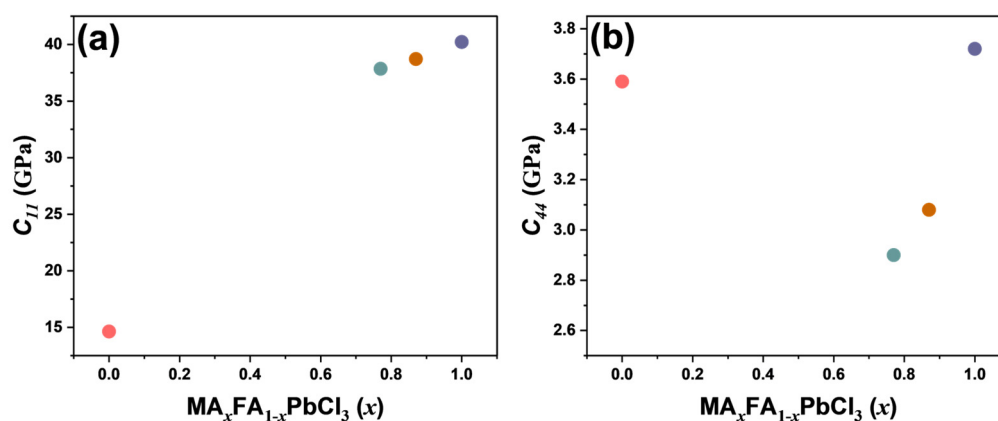


Figure 7. (a) C_{11} and (b) C_{44} elastic constants as a function of composition x in $\text{MA}_x\text{FA}_{1-x}\text{PbCl}_3$ ($x = 1, 0.87, 0.77$) single crystals. (DFT values of FAPbCl₃ are from ref. [34]).

Table 3. Summary of calculated sound velocities and elastic constants for $\text{MA}_x\text{FA}_{1-x}\text{PbCl}_3$ ($x = 1, 0.87, 0.77$) single crystals. Values of elastic constants for pure FAPbCl₃ were from ref [34].

Composition	V_{LA} (m/s)	V_{TA} (m/s)	C_{11} (GPa)	C_{44} (GPa)
MAPbCl ₃ (Brillouin)	3574	1087	40.22	3.72
MA _{0.87} FA _{0.13} PbCl ₃ (Brillouin)	3507	990	38.71	3.08
MA _{0.77} FA _{0.23} PbCl ₃ (Brillouin)	3471	961	37.85	2.90
FAPbCl ₃ (DFT calculation)	-	-	14.64 [34]	3.59 [34]

The incorporation of larger FA⁺ cations distorts the lattice, resulting in a monotonic decrease in both elastic constants and sound velocities in the mixed system. A recent study has suggested that the FA cations in FAPbBr₃ have weaker hydrogen bonding between H atoms and halide ions compared to that between MA cations and halide ions in MAPbBr₃ [67]. This suggests that the larger cation size of FA may distort the crystal structure and weaken the bonding between FA cations and halide ions as the FA

concentration increases. This results in increased Pb-Cl bond length and weaker bond strength in the inorganic framework of halide perovskites, leading to greater flexibility and lower elastic moduli. Conversely, the smaller MA cations are likely to contribute to stronger elastic interactions, hence, pure MAPbCl₃ shows the highest value for the sound velocity and the associated elastic constants. Figure 7 shows that the DFT results are deviating significantly from the changing trend of the experimental elastic constants, indicating that the DFT approach needs to be refined to get more reliable results of elastic properties.

The absorption coefficient (α) was calculated from the full width at half maximum (FWHM, Γ_B) of the LA and TA modes using the following formula:

$$\alpha = \frac{\pi\Gamma_B}{V} \quad (3)$$

The calculated absorption coefficients for both acoustic modes, as shown in Figure 8, show a consistent decrease with increasing FA content. This trend indicates that materials with higher FA content have lower absorption or attenuation coefficients, implying a weaker presence of damping effects or internal friction. This could be due to the larger ionic radii and lower polarizability of the FA cation, which could potentially lead to a weaker interaction with the inorganic framework and a smaller bandgap. In addition, the heterogeneity introduced via the MA/FA random substitution is much smaller than the wavelength of LA and TA mode (the order of 100 nm) and, thus, does not affect the acoustic absorption process. These results highlight the importance of investigating how changes in composition not only affect the mechanical properties but also shape the mechanisms of energy dissipation within the MA_xFA_{1-x}PbCl₃ mixed halide perovskite system.

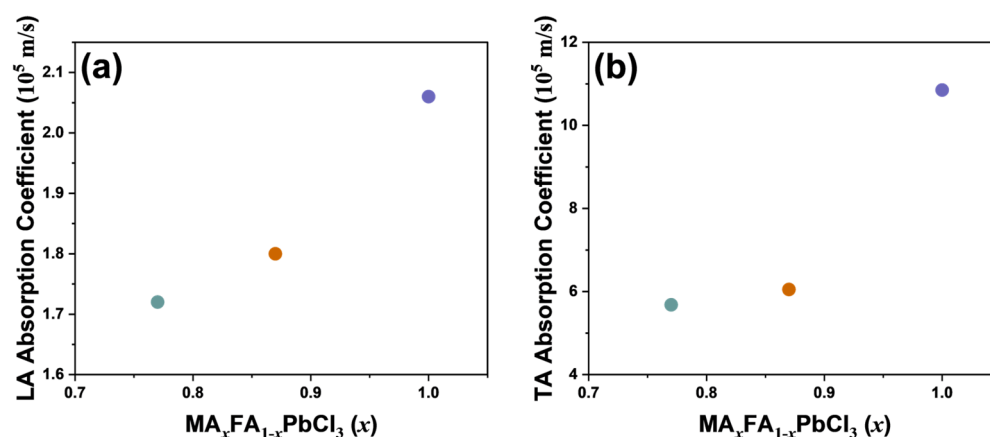


Figure 8. (a) Longitudinal acoustic (LA) and (b) transverse acoustic (TA) absorption coefficients as a function of composition x in MA _{x} FA_{1- x} PbCl₃ ($x = 1, 0.87, 0.77$) single crystals.

3. Materials and Methods

3.1. Chemicals

Lead chloride (PbCl₂, 99.999%), methylamine (CH₃NH₂, 40% in water), hydrochloric acid (HCl, 37%, ACS reagent), formamidinium chloride (CH(NH₂)₂Cl, 99.9%), dimethyl sulfoxide (DMSO, anhydrous $\geq 99.9\%$), diethyl ether (HPLC grade, $\geq 99.9\%$), and ethanol (anhydrous 99.5%) were purchased from Sigma Aldrich (St. Louis, MO, USA). Methylammonium chloride (MACl) was synthesized according to previously reported methods [26].

3.2. Single Crystals Synthesis

The MA _{x} FA_{1- x} PbCl₃ ($x = 1, 0.7, 0.6$) single crystals were synthesized using the solvent evaporation method. The MAcl, PbCl₂, and FAcI powders were dissolved in DMSO (10 mL) in equimolar ratios at 40 °C with continuous stirring in a glove box under nitrogen gas environment. The resulting dissolved solution was filtered into a crystallization dish using a 0.22 μ m syringe filter. Slow evaporation was promoted by covering the dish with

aluminum foil and leaving it undisturbed at a constant temperature of 85 °C for 1–2 days. Transparent $\text{MA}_x\text{FA}_{1-x}\text{PbCl}_3$ ($x = 1, 0.7, 0.6$) single crystals were formed, which were then washed with dichloromethane and dried in a vacuum oven at 60 °C for 12 h to obtain the final product.

3.3. Characterization Techniques

In this study, the powder XRD pattern was obtained using a high-resolution XRD spectrometer (PANalytical; X'pert PRO MPD, Malvern, UK) at room temperature with Cu-K radiation ($\lambda = 1.5406 \text{ \AA}$) in the 2θ angular range from 10 to 60°. Prior to measurement, the single crystals were crushed into crystalline powders. The obtained XRD patterns were analyzed using the PANalytical software (X'pert highscore v1.1) for further analysis.

Moreover, ^1H solid-state room-temperature NMR spectra were acquired on a ($^1\text{H} = 400.13 \text{ MHz}$) Bruker Avance II+ spectrometer using TopSpin 2.1 software (at KBSI Seoul Western Center, Seoul, Republic of Korea); spectra were collected with a 4 mm magic-angle spinning (MAS) probe under 12 kHz spinning conditions. Quantitative ^1H single pulse experiments were performed with a pulse length of 1.2 μs , a recycle delay of 100, and 8 scans. The pulse length and recycle delay were carefully calibrated prior to acquisition of the final spectra to ensure full relaxation of the magnetization and to meet the conditions for quantitative data acquisition. Tetramethylsilane (TMS) was used as a calibration sample. The analysis of the obtained data was carried out using the MestReNova program.

Raman measurements were conducted using a standard Raman spectrometer (LabRam HR800, Horiba Co., Kyoto, Japan) in the frequency range of 10 to 3500 cm^{-1} . A diode-pumped solid-state green laser with a wavelength of 532 nm was utilized to probe the samples. Backscattering geometry was used in terms of an optical microscope (BX41, Olympus, Tokyo, Japan) with a 50 \times magnification objective lens. The phonon propagation direction for the measurement was [100] in the cubic phase. Prior to measurement, the Raman spectrometer was calibrated using a silicon substrate as a reference sample with a single peak at 520 cm^{-1} . The measured Raman spectra were corrected using the Bose-Einstein correction factor.

Brillouin spectra were acquired using a standard tandem multi-pass Fabry–Perot interferometer (TFP-2, JRS Co., Zurich, Switzerland) with a 532 nm excitation source. A modified microscope with a backscattering geometry (BH-2, Olympus, Tokyo, Japan) was used for the measurement. The signal was identified and averaged over 1024 channels using a conventional photon-counting instrument linked with a multichannel analyzer. The free spectral range was set to 33 GHz to include both the LA and the TA modes in the Brillouin spectrum.

4. Conclusions

The mixed halide perovskite single crystals $\text{MA}_x\text{FA}_{1-x}\text{PbCl}_3$ have been grown successfully, providing valuable insights into their structural, vibrational, and elastic properties. Solid-state ^1H NMR spectroscopy revealed that the actual composition of the grown crystals differed significantly from the nominal values. This highlights the importance of controlling the composition after synthesis. Powder X-ray diffraction analysis confirmed the uniform crystallographic structure of the synthesized compounds, which maintained the cubic symmetry common to MAPbCl_3 and FAPbCl_3 . The inclusion of FA cations led to an increase in the lattice constant, the unit cell volume, and a decrease in the density, indicating structural changes due to FA substitution. Raman spectroscopy revealed wavenumber shifts in the vibrational modes and the appearance of new modes, particularly associated with the FA cations, indicating the successful incorporation of the FA cations into the lattice structure and local structural distortions caused by them. These distortions may be attributed to the different ionic radii and interactions of the FA and MA cations with the PbCl_6 octahedra.

Brillouin scattering results showed that the incorporation of the FA cation induced a monotonic decrease in both the longitudinal and transverse sound velocities, along with the corresponding elastic constants, ultimately affecting the elasticity of the perovskite

framework. It suggests that incorporating different cations in the perovskite lattice is one way to control the elastic properties of this system. The obtained absorption coefficients show that the mixed crystals with higher FA content have lower absorption coefficients, indicating reduced damping effects and internal friction. This may be due to weaker interactions between FA cations and the inorganic framework. In summary, our study highlights the complex relationship between the composition and physical properties of $MA_xFA_{1-x}PbCl_3$ mixed halide perovskites. These findings are not only relevant to their potential use in optoelectronic devices but also improve our fundamental understanding of these materials. Further research is needed to fully explore their range of properties and improve their functionality.

Supplementary Materials: The following supporting information can be downloaded at: <https://www.mdpi.com/article/10.3390/inorganics11100416/s1>, Figure S1: Raman spectra and best-fitted curves of MAPbCl₃ single crystal at room temperature. Figure S2: Raman spectra and best-fitted curves of MA_{0.87}FA_{0.13}PbCl₃ single crystal at room temperature. Figure S3: Raman spectra and best-fitted curves of MA_{0.77}FA_{0.23}PbCl₃ single crystal at room temperature. Figure S4: Interpolated refractive indices for MA_xFA_{1-x}PbCl₃ single crystals.

Author Contributions: Methodology, S.B.J. and J.-H.K.; Validation, S.B.J. and F.H.N.; Formal analysis, S.B.J. and F.H.N.; Investigation, S.B.J. and F.H.N.; Resources, J.-H.K.; Data curation, S.B.J. and F.H.N.; Writing—original draft, S.B.J.; Writing—review and editing, J.-H.K.; Visualization, S.B.J.; Supervision, J.-H.K.; Project administration, J.-H.K.; Funding acquisition, J.-H.K. All authors have read and agreed to the published version of the manuscript.

Funding: This work was supported by the National Research Foundation of Korea (NRF) grant funded by the Korea government (MSIT) (No. RS-2023-00219703).

Data Availability Statement: The data in this study are available upon request to the corresponding author.

Conflicts of Interest: The authors declare no conflict of interest.

References

1. Quan, L.N.; Rand, B.P.; Friend, R.H.; Mhaisalkar, S.G.; Lee, T.W.; Sargent, E.H. Perovskites for Next-Generation Optical Sources. *Chem. Rev.* **2019**, *119*, 7444–7477. [[CrossRef](#)] [[PubMed](#)]
2. Maćzka, M.; Ptak, M.; Gaĝor, A.; Stefańska, D.; Sieradzki, A. Layered Lead Iodide of [Methylhydrazinium]₂PbI₄ with a Reduced Band Gap: Thermochromic Luminescence and Switchable Dielectric Properties Triggered by Structural Phase Transitions. *Chem. Mater.* **2019**, *31*, 8563–8575. [[CrossRef](#)]
3. Li, X.; Hoffman, J.M.; Kanatzidis, M.G. The 2D halide perovskite rulebook: How the spacer influences everything from the structure to optoelectronic device efficiency. *Chem. Rev.* **2021**, *121*, 2230–2291. [[CrossRef](#)] [[PubMed](#)]
4. Maćzka, M.; Zaręba, J.K.; Gaĝor, A.; Stefańska, D.; Ptak, M.; Roleder, K.; Kajewski, D.; Soszyński, A.; Fedoruk, K.; Sieradzki, A. [Methylhydrazinium]₂PbBr₄, a Ferroelectric Hybrid Organic-Inorganic Perovskite with Multiple Nonlinear Optical Outputs. *Chem. Mater.* **2021**, *33*, 2331–2342. [[CrossRef](#)]
5. Maćzka, M.; Gaĝor, A.; Stroppa, A.; Gonçalves, J.N.; Zaręba, J.K.; Stefańska, D.; Pikul, A.; Drozd, M.; Sieradzki, A. Two-dimensional metal dicyanamide frameworks of BeTriMe[M(dca)₃(H₂O)] (BeTriMe = benzyltrimethylammonium; dca = dicyanamide; M = Mn²⁺, Co²⁺, Ni²⁺): Coexistence of polar and magnetic orders and nonlinear optical threshold temperature sensing. *J. Mater. Chem. C* **2020**, *8*, 11735–11747. [[CrossRef](#)]
6. Maćzka, M.; Zienkiewicz, J.A.; Ptak, M. Comparative Studies of Phonon Properties of Three-Dimensional Hybrid Organic-Inorganic Perovskites Comprising Methylhydrazinium, Methylammonium, and Formamidinium Cations. *J. Phys. Chem. C* **2022**, *126*, 4048–4056. [[CrossRef](#)]
7. Grätzel, M. The light and shade of perovskite solar cells. *Nat. Mater.* **2014**, *13*, 838–842. [[CrossRef](#)]
8. Šimėnas, M.; Balčiūnas, S.; Gaĝor, A.; Pieniāzek, A.; Tolborg, K.; Kinka, M.; Klimavicius, V.; Svirskas, Š.N.; Kalendra, V.; Ptak, M.; et al. Mixology of MA_{1-x}EA_xPbI₃ Hybrid Perovskites: Phase Transitions, Cation Dynamics, and Photoluminescence. *Chem. Mater.* **2022**, *34*, 10104–10112. [[CrossRef](#)]
9. Glazer, A.M. Simple ways of determining perovskite structures. *Acta Crystallogr. Sect. A* **1975**, *31*, 756–762. [[CrossRef](#)]
10. Petrov, A.A.; Goodilin, E.A.; Tarasov, A.B.; Lazarenko, V.A.; Dorovatovskii, P.V.; Khrustalev, V.N. Formamidinium iodide: Crystal structure and phase transitions. *Acta Crystallogr. Sect. E Crystallogr. Commun.* **2017**, *73*, 569–572. [[CrossRef](#)]
11. Ruan, S.; McMeekin, D.P.; Fan, R.; Webster, N.A.S.; Ebendorff-Heidepriem, H.; Cheng, Y.B.; Lu, J.; Ruan, Y.; McNeill, C.R. Raman Spectroscopy of Formamidinium-Based Lead Halide Perovskite Single Crystals. *J. Phys. Chem. C* **2020**, *124*, 2265–2272. [[CrossRef](#)]

12. Snaith, H.J. Perovskites: The emergence of a new era for low-cost, high-efficiency solar cells. *J. Phys. Chem. Lett.* **2013**, *4*, 3623–3630. [[CrossRef](#)]
13. Kojima, A.; Teshima, K.; Shirai, Y.; Miyasaka, T. Organometal halide perovskites as visible-light sensitizers for photovoltaic cells. *J. Am. Chem. Soc.* **2009**, *131*, 6050–6051. [[CrossRef](#)] [[PubMed](#)]
14. Park, N.G. Organometal perovskite light absorbers toward a 20% efficiency low-cost solid-state mesoscopic solar cell. *J. Phys. Chem. Lett.* **2013**, *4*, 2423–2429. [[CrossRef](#)]
15. Li, Z.; Klein, T.R.; Kim, D.H.; Yang, M.; Berry, J.J.; Van Hest, M.F.A.M.; Zhu, K. Scalable fabrication of perovskite solar cells. *Nat. Rev. Mater.* **2018**, *3*, 18017. [[CrossRef](#)]
16. Jeong, J.; Kim, M.; Seo, J.; Lu, H.; Ahlawat, P.; Mishra, A.; Yang, Y.; Hope, M.A.; Eickemeyer, F.T.; Kim, M.; et al. Pseudo-halide anion engineering for α -FAPbI₃ perovskite solar cells. *Nature* **2021**, *592*, 381–385. [[CrossRef](#)] [[PubMed](#)]
17. Yoo, J.J.; Seo, G.; Chua, M.R.; Park, T.G.; Lu, Y.; Rotermund, F.; Kim, Y.K.; Moon, C.S.; Jeon, N.J.; Correa-Baena, J.P.; et al. Efficient perovskite solar cells via improved carrier management. *Nature* **2021**, *590*, 587–593. [[CrossRef](#)]
18. Frost, J.M.; Butler, K.T.; Brivio, F.; Hendon, C.H.; Van Schilfgaarde, M.; Walsh, A. Atomistic origins of high-performance in hybrid halide perovskite solar cells. *Nano Lett.* **2014**, *14*, 2584–2590. [[CrossRef](#)]
19. Frost, J.M.; Walsh, A. What Is Moving in Hybrid Halide Perovskite Solar Cells? *Acc. Chem. Res.* **2016**, *49*, 528–535. [[CrossRef](#)]
20. Egger, D.A.; Rappe, A.M.; Kronik, L. Hybrid Organic-Inorganic Perovskites on the Move. *Acc. Chem. Res.* **2016**, *49*, 573–581. [[CrossRef](#)] [[PubMed](#)]
21. Pang, S.; Hu, H.; Zhang, J.; Lv, S.; Yu, Y.; Wei, F.; Qin, T.; Xu, H.; Liu, Z.; Cui, G. NH₂CH=NH₂PbI₃: An alternative organolead iodide perovskite sensitizer for mesoscopic solar cells. *Chem. Mater.* **2014**, *26*, 1485–1491. [[CrossRef](#)]
22. Eperon, G.E.; Stranks, S.D.; Menelaou, C.; Johnston, M.B.; Herz, L.M.; Snaith, H.J. Formamidinium lead trihalide: A broadly tunable perovskite for efficient planar heterojunction solar cells. *Energy Environ. Sci.* **2014**, *7*, 982–988. [[CrossRef](#)]
23. Pellet, N.; Gao, P.; Gregori, G.; Yang, T.Y.; Nazeeruddin, M.K.; Maier, J.; Grätzel, M. Mixed-organic-cation perovskite photovoltaics for enhanced solar-light harvesting. *Angew. Chem. Int. Ed.* **2014**, *53*, 3151–3157. [[CrossRef](#)]
24. Levchuk, I.; Osvet, A.; Tang, X.; Brandl, M.; Perea, J.D.; Hoegl, F.; Matt, G.J.; Hock, R.; Batentschuk, M.; Brabec, C.J. Brightly Luminescent and Color-Tunable Formamidinium Lead Halide Perovskite FAPbX₃ (X = Cl, Br, I) Colloidal Nanocrystals. *Nano Lett.* **2017**, *17*, 2765–2770. [[CrossRef](#)]
25. Cheng, Z.; Liu, K.; Yang, J.; Chen, X.; Xie, X.; Li, B.; Zhang, Z.; Liu, L.; Shan, C.; Shen, D. High-Performance Planar-Type Ultraviolet Photodetector Based on High-Quality CH₃NH₃PbCl₃ Perovskite Single Crystals. *ACS Appl. Mater. Interfaces* **2019**, *11*, 34144–34150. [[CrossRef](#)] [[PubMed](#)]
26. Naqvi, F.H.; Ko, J.H. Structural Phase Transitions and Thermal Degradation Process of MAPbCl₃ Single Crystals Studied by Raman and Brillouin Scattering. *Materials* **2022**, *15*, 8151. [[CrossRef](#)] [[PubMed](#)]
27. Lee, J.; Naqvi, F.; Ko, J.H.; Kim, T.; Ahn, C. Acoustic Anomalies and the Critical Slowing-Down Behavior of MAPbCl₃ Single Crystals Studied by Brillouin Light Scattering. *Materials* **2022**, *15*, 3692. [[CrossRef](#)] [[PubMed](#)]
28. Parfenov, A.A.; Yamilova, O.R.; Gutsev, L.G.; Sagdullina, D.K.; Novikov, A.V.; Ramachandran, B.R.; Stevenson, K.J.; Aldoshin, S.M.; Troshin, P.A. Highly sensitive and selective ammonia gas sensor based on FAPbCl₃ lead halide perovskites. *J. Mater. Chem. C* **2021**, *9*, 2561–2568. [[CrossRef](#)]
29. Wang, J.; Peng, J.; Sun, Y.; Liu, X.; Chen, Y.; Liang, Z. FAPbCl₃ Perovskite as Alternative Interfacial Layer for Highly Efficient and Stable Polymer Solar Cells. *Adv. Electron. Mater.* **2016**, *2*, 1600329. [[CrossRef](#)]
30. Gong, J.; Li, X.; Guo, P.; Zhang, L.; Huang, W.; Lu, K.; Cheng, Y.; Schaller, R.D.; Marks, T.J.; Xu, T. Energy-distinguishable bipolar UV photoelectron injection from LiCl-promoted FAPbCl₃ perovskite nanorods. *J. Mater. Chem. A* **2019**, *7*, 13043–13049. [[CrossRef](#)]
31. Govinda, S.; Kore, B.P.; Swain, D.; Hossain, A.; De, C.; Guru Row, T.N.; Sarma, D.D. Critical Comparison of FAPbX₃ and MAPbX₃ (X = Br and Cl): How Do They Differ? *J. Phys. Chem. C* **2018**, *122*, 13758–13766. [[CrossRef](#)]
32. Sharma, V.K.; Mukhopadhyay, R.; Mohanty, A.; García Sakai, V.; Tyagi, M.; Sarma, D.D. Influence of the Halide Ion on the A-Site Dynamics in FAPbX₃ (X = Br and Cl). *J. Phys. Chem. C* **2022**, *126*, 7158–7168. [[CrossRef](#)]
33. Nations, S.; Gutsev, L.; Ramachandran, B.; Aldoshin, S.; Duan, Y.; Wang, S. First-principles study of the defect-activity and optical properties of FAPbCl₃. *Mater. Adv.* **2022**, *3*, 3897–3905. [[CrossRef](#)]
34. Roknuzzaman, M.; Alarco, J.A.; Wang, H.; Du, A.; Tesfamichael, T.; Ostrikov, K.K. Ab initio atomistic insights into lead-free formamidinium based hybrid perovskites for photovoltaics and optoelectronics. *Comput. Mater. Sci.* **2019**, *169*, 109118. [[CrossRef](#)]
35. Pachori, S.; Agarwal, R.; Shukla, A.; Rani, U.; Verma, A.S. Mechanically stable with highly absorptive formamidinium lead halide perovskites [(HC(NH₂)₂PbX₃; X = Br, Cl]: Recent advances and perspectives. *Int. J. Quantum Chem.* **2021**, *121*, e26671. [[CrossRef](#)]
36. Yang, W.S.; Noh, J.H.; Jeon, N.J.; Kim, Y.C.; Ryu, S.; Seo, J.; Seok, S. II High-performance photovoltaic perovskite layers fabricated through intramolecular exchange. *Science* **2015**, *348*, 1234–1237. [[CrossRef](#)]
37. Charles, B.; Dillon, J.; Weber, O.J.; Islam, M.S.; Weller, M.T. Understanding the stability of mixed A-cation lead iodide perovskites. *J. Mater. Chem. A* **2017**, *5*, 22495–22499. [[CrossRef](#)]
38. Lee, J.W.; Kim, D.H.; Kim, H.S.; Seo, S.W.; Cho, S.M.; Park, N.G. Formamidinium and cesium hybridization for photo- and moisture-stable perovskite solar cell. *Adv. Energy Mater.* **2015**, *5*, 1501310. [[CrossRef](#)]
39. Yi, C.; Luo, J.; Meloni, S.; Boziki, A.; Ashari-Astani, N.; Grätzel, C.; Zakeeruddin, S.M.; Röthlisberger, U.; Grätzel, M. Entropic stabilization of mixed A-cation ABX₃ metal halide perovskites for high performance perovskite solar cells. *Energy Environ. Sci.* **2016**, *9*, 656–662. [[CrossRef](#)]

40. Saliba, M.; Matsui, T.; Domanski, K.; Seo, J.Y.; Ummadisingu, A.; Zakeeruddin, S.M.; Correa-Baena, J.P.; Tress, W.R.; Abate, A.; Hagfeldt, A.; et al. Incorporation of rubidium cations into perovskite solar cells improves photovoltaic performance. *Science* **2016**, *354*, 203–206. [[CrossRef](#)]
41. Saliba, M.; Matsui, T.; Seo, J.Y.; Domanski, K.; Correa-Baena, J.P.; Nazeeruddin, M.K.; Zakeeruddin, S.M.; Tress, W.; Abate, A.; Hagfeldt, A.; et al. Cesium-containing triple cation perovskite solar cells: Improved stability, reproducibility and high efficiency. *Energy Environ. Sci.* **2016**, *9*, 1989–1997. [[CrossRef](#)]
42. Weber, O.J.; Charles, B.; Weller, M.T. Phase behaviour and composition in the formamidinium-methylammonium hybrid lead iodide perovskite solid solution. *J. Mater. Chem. A* **2016**, *4*, 15375–15382. [[CrossRef](#)]
43. Jesper Jacobsson, T.; Correa-Baena, J.P.; Pazoki, M.; Saliba, M.; Schenk, K.; Grätzel, M.; Hagfeldt, A. Exploration of the compositional space for mixed lead halogen perovskites for high efficiency solar cells. *Energy Environ. Sci.* **2016**, *9*, 1706–1724. [[CrossRef](#)]
44. Yang, Z.; Chueh, C.C.; Liang, P.W.; Crump, M.; Lin, F.; Zhu, Z.; Jen, A.K.Y. Effects of formamidinium and bromide ion substitution in methylammonium lead triiodide toward high-performance perovskite solar cells. *Nano Energy* **2016**, *22*, 328–337. [[CrossRef](#)]
45. Pisanu, A.; Ferrara, C.; Quadrelli, P.; Guizzetti, G.; Patrini, M.; Milanese, C.; Tealdi, C.; Malavasi, L. The FA_{1-x}MA_xPbI₃ System: Correlations among Stoichiometry Control, Crystal Structure, Optical Properties, and Phase Stability. *J. Phys. Chem. C* **2017**, *121*, 8746–8751. [[CrossRef](#)]
46. Alonso, M.I.; Charles, B.; Francisco-López, A.; Garriga, M.; Weller, M.T.; Goñi, A.R. Spectroscopic ellipsometry study of FA_xMA_{1-x}PbI₃ hybrid perovskite single crystals. *J. Vac. Sci. Technol. B* **2019**, *37*, 062901. [[CrossRef](#)]
47. Francisco-López, A.; Charles, B.; Alonso, M.I.; Garriga, M.; Campoy-Quiles, M.; Weller, M.T.; Goñi, A.R. Phase Diagram of Methylammonium/Formamidinium Lead Iodide Perovskite Solid Solutions from Temperature-Dependent Photoluminescence and Raman Spectroscopies. *J. Phys. Chem. C* **2020**, *124*, 3448–3458. [[CrossRef](#)]
48. Chen, T.; Chen, W.L.; Foley, B.J.; Lee, J.; Ruff, J.P.C.; Ko, J.Y.P.; Brown, C.M.; Harriger, L.W.; Zhang, D.; Park, C.; et al. Origin of long lifetime of band-edge charge carriers in organic–inorganic lead iodide perovskites. *Proc. Natl. Acad. Sci. USA* **2017**, *114*, 7519–7524. [[CrossRef](#)]
49. Miyata, A.; Mitioglu, A.; Plochocka, P.; Portugall, O.; Wang, J.T.W.; Stranks, S.D.; Snaith, H.J.; Nicholas, R.J. Direct measurement of the exciton binding energy and effective masses for charge carriers in organic-inorganic tri-halide perovskites. *Nat. Phys.* **2015**, *11*, 582–587. [[CrossRef](#)]
50. Chen, T.; Foley, B.J.; Park, C.; Brown, C.M.; Harriger, L.W.; Lee, J.; Ruff, J.; Yoon, M.; Choi, J.J.; Lee, S.H. Entropy-driven structural transition and kinetic trapping in formamidinium lead iodide perovskite. *Sci. Adv.* **2016**, *2*, e1601650. [[CrossRef](#)]
51. Stoumpos, C.C.; Malliakas, C.D.; Kanatzidis, M.G. Semiconducting tin and lead iodide perovskites with organic cations: Phase transitions, high mobilities, and near-infrared photoluminescent properties. *Inorg. Chem.* **2013**, *52*, 9019–9038. [[CrossRef](#)] [[PubMed](#)]
52. Jeon, N.J.; Noh, J.H.; Yang, W.S.; Kim, Y.C.; Ryu, S.; Seo, J.; Seok, S. II Compositional engineering of perovskite materials for high-performance solar cells. *Nature* **2015**, *517*, 476–480. [[CrossRef](#)] [[PubMed](#)]
53. Binek, A.; Hanusch, F.C.; Docampo, P.; Bein, T. Stabilization of the trigonal high-temperature phase of formamidinium lead iodide. *J. Phys. Chem. Lett.* **2015**, *6*, 1249–1253. [[CrossRef](#)] [[PubMed](#)]
54. Šimėnas, M.; Balčiūnas, S.; Svirskas, Š.N.; Kinka, M.; Ptak, M.; Kalendra, V.; Gagor, A.; Szewczyk, D.; Sieradzki, A.; Grigalaitis, R.; et al. Phase Diagram and Cation Dynamics of Mixed MA_{1-x}FA_xPbBr₃ Hybrid Perovskites. *Chem. Mater.* **2021**, *33*, 5926–5934. [[CrossRef](#)]
55. Baikie, T.; Barrow, N.S.; Fang, Y.; Keenan, P.J.; Slater, P.R.; Piltz, R.O.; Gutmann, M.; Mhaisalkar, S.G.; White, T.J. A combined single crystal neutron/X-ray diffraction and solid-state nuclear magnetic resonance study of the hybrid perovskites CH₃NH₃PbX₃ (X = I, Br and Cl). *J. Mater. Chem. A* **2015**, *3*, 9298–9307. [[CrossRef](#)]
56. Maculan, G.; Sheikh, A.D.; Abdelhady, A.L.; Saidaminov, M.I.; Haque, M.A.; Murali, B.; Alarousu, E.; Mohammed, O.F.; Wu, T.; Bakr, O.M. CH₃NH₃PbCl₃ Single Crystals: Inverse Temperature Crystallization and Visible-Blind UV-Photodetector. *J. Phys. Chem. Lett.* **2015**, *6*, 3781–3786. [[CrossRef](#)]
57. Askar, A.M.; Karmakar, A.; Bernard, G.M.; Ha, M.; Terskikh, V.V.; Wiltshire, B.D.; Patel, S.; Fleet, J.; Shankar, K.; Michaelis, V.K. Composition-Tunable Formamidinium Lead Mixed Halide Perovskites via Solvent-Free Mechanochemical Synthesis: Decoding the Pb Environments Using Solid-State NMR Spectroscopy. *J. Phys. Chem. Lett.* **2018**, *9*, 2671–2677. [[CrossRef](#)] [[PubMed](#)]
58. He, C.; Zha, G.; Deng, C.; An, Y.; Mao, R.; Liu, Y.; Lu, Y.; Chen, Z. Refractive Index Dispersion of Organic–Inorganic Hybrid Halide Perovskite CH₃NH₃PbX₃ (X = Cl, Br, I) Single Crystals. *Cryst. Res. Technol.* **2019**, *54*, 1900011. [[CrossRef](#)]
59. Niemann, R.G.; Kontos, A.G.; Palles, D.; Kamitsos, E.I.; Kaltzoglou, A.; Brivio, F.; Falaras, P.; Cameron, P.J. Halogen Effects on Ordering and Bonding of CH₃NH₃⁺ in CH₃NH₃PbX₃ (X = Cl, Br, I) Hybrid Perovskites: A Vibrational Spectroscopic Study. *J. Phys. Chem. C* **2016**, *120*, 2509–2519. [[CrossRef](#)]
60. Kucharska, E.; Hanuza, J.; Ciupa, A.; Mączka, M.; Macalik, L. Vibrational properties and DFT calculations of formamidinium-templated Co and Fe formates. *Vib. Spectrosc.* **2014**, *75*, 45–50. [[CrossRef](#)]
61. Kontos, A.G.; Manolis, G.K.; Kaltzoglou, A.; Palles, D.; Kamitsos, E.I.; Kanatzidis, M.G.; Falaras, P. Halogen-NH₂⁺ Interaction, Temperature-Induced Phase Transition, and Ordering in (NH₂CHNH₂)PbX₃ (X = Cl, Br, I) Hybrid Perovskites. *J. Phys. Chem. C* **2020**, *124*, 8479–8487. [[CrossRef](#)]

62. Leguy, A.M.A.; Goñi, A.R.; Frost, J.M.; Skelton, J.; Brivio, F.; Rodríguez-Martínez, X.; Weber, O.J.; Pallipurath, A.; Alonso, M.I.; Campoy-Quiles, M.; et al. Dynamic disorder, phonon lifetimes, and the assignment of modes to the vibrational spectra of methylammonium lead halide perovskites. *Phys. Chem. Chem. Phys.* **2016**, *18*, 27051–27066. [[CrossRef](#)]
63. Maalej, A.; Abid, Y.; Kallel, A.; Daoud, A.; Lautié, A.; Romain, F. Phase transitions and crystal dynamics in the cubic perovskite- $\text{CH}_3\text{NH}_3\text{PbCl}_3$. *Solid State Commun.* **1997**, *103*, 279–284. [[CrossRef](#)]
64. Maćzka, M.; Ptak, M.; Vasconcelos, D.L.M.; Giriunas, L.; Freire, P.T.C.; Bertmer, M.; Banyś, J.; Simenas, M. NMR and Raman Scattering Studies of Temperature- and Pressure-Driven Phase Transitions in $\text{CH}_3\text{NH}_2\text{NH}_2\text{PbCl}_3$ Perovskite. *J. Phys. Chem. C* **2020**, *124*, 26999–27008. [[CrossRef](#)]
65. Glaser, T.; Müller, C.; Sendner, M.; Krekeler, C.; Semonin, O.E.; Hull, T.D.; Yaffe, O.; Owen, J.S.; Kowalsky, W.; Pucci, A.; et al. Infrared Spectroscopic Study of Vibrational Modes in Methylammonium Lead Halide Perovskites. *J. Phys. Chem. Lett.* **2015**, *6*, 2913–2918. [[CrossRef](#)] [[PubMed](#)]
66. Ma, L.; Li, W.; Yang, K.; Bi, J.; Feng, J.; Zhang, J.; Yan, Z.; Zhou, X.; Liu, C.; Ji, Y.; et al. A- or X-site mixture on mechanical properties of APbX_3 perovskite single crystals. *APL Mater.* **2021**, *9*, 041112. [[CrossRef](#)]
67. Sun, S.; Isikgor, F.H.; Deng, Z.; Wei, F.; Kieslich, G.; Bristowe, P.D.; Ouyang, J.; Cheetham, A.K. Factors Influencing the Mechanical Properties of Formamidinium Lead Halides and Related Hybrid Perovskites. *ChemSusChem* **2017**, *10*, 3740–3745. [[CrossRef](#)] [[PubMed](#)]

Disclaimer/Publisher’s Note: The statements, opinions and data contained in all publications are solely those of the individual author(s) and contributor(s) and not of MDPI and/or the editor(s). MDPI and/or the editor(s) disclaim responsibility for any injury to people or property resulting from any ideas, methods, instructions or products referred to in the content.